

Interpreting LOFAR 21-cm signal upper limits at $z \approx 9.1$ in the context of high- z galaxy and reionisation observations

Bradley Greig^{1,2*}, Andrei Mesinger³, Léon V. E. Koopmans⁴, Benedetta Ciardi⁵, Garrelt Mellema⁶, Saleem Zaroubi^{7,8,4}, Sambit K. Giri⁹, Raghunath Ghara^{7,8}, Abhik Ghosh¹⁰, Ilian T. Iliev¹¹, Florent G. Mertens^{4,12}, Rajesh Mondal^{6,11}, André R. Offringa^{4,13}, Vishambhar N. Pandey^{4,13}

¹ARC Centre of Excellence for All-Sky Astrophysics in 3 Dimensions (ASTRO 3D), University of Melbourne, VIC 3010, Australia

²School of Physics, University of Melbourne, Parkville, VIC 3010, Australia

³Scuola Normale Superiore, Piazza dei Cavalieri 7, I-56126 Pisa, Italy

⁴Kapteyn Astronomical Institute, University of Groningen, PO Box 800, 9700 AV Groningen, The Netherlands

⁵Max-Planck Institute for Astrophysics, Karl-Schwarzschild-Straße 1, D-85748 Garching, Germany

⁶The Oskar Klein Centre, Department of Astronomy, Stockholm University, AlbaNova, SE-10691 Stockholm, Sweden

⁷Department of Natural Sciences, The Open University of Israel, 1 University Road, PO Box 808, Ra'anana 4353701, Israel

⁸Department of Physics, Technion, Haifa 32000, Israel

⁹Institute for Computational Science, University of Zurich, Winterthurerstrasse 190, 8057 Zurich, Switzerland

¹⁰Department of Physics, Banwarilal Bhalotia College, GT Rd, Ushagram, Asansol, West Bengal 713303, India

¹¹Astronomy Centre, Department of Physics and Astronomy, Pevensey II Building, University of Sussex, Brighton BN1 9QH, UK

¹²LERMA, Observatoire de Paris, PSL Research University, CNRS, Sorbonne Université, F-75014 Paris, France

¹³ASTRON – the Netherlands Institute for Radio Astronomy, Oude Hoogeveensedijk 4, 7991 PD Dwingeloo, The Netherlands

8 June 2020

ABSTRACT

Using the latest upper limits on the 21-cm power spectrum at $z \approx 9.1$ from the Low Frequency Array (LOFAR), we explore regions of parameter space which are inconsistent with the data. We use 21CMMC, a Monte Carlo Markov Chain sampler of 21CMFAST which directly forward models the 3D cosmic 21-cm signal in a fully Bayesian framework. We use the astrophysical parameterisation from 21CMFAST, which includes mass-dependent star formation rates and ionising escape fractions as well as soft-band X-ray luminosities to place limits on the properties of the high- z galaxies. Further, we connect the disfavoured regions of parameter space with existing observational constraints on the Epoch of Reionisation such as ultra-violet (UV) luminosity functions, background UV photoionisation rate, intergalactic medium (IGM) neutral fraction and the electron scattering optical depth. We find that all models exceeding the 21-cm signal limits set by LOFAR at $z \approx 9.1$ are excluded at $\gtrsim 2\sigma$ by other probes. Finally, we place limits on the IGM spin temperature from LOFAR, disfavoured at 95 per cent confidence spin temperatures below ~ 2.6 K across an IGM neutral fraction range of $0.15 \lesssim \bar{x}_{\text{HI}} \lesssim 0.6$. Note, these limits are only obtained from 141 hrs of data in a single redshift bin. With tighter upper limits, across multiple redshift bins expected in the near future from LOFAR, more viable models will be ruled out. Our approach demonstrates the potential of forward modelling tools such as 21CMMC in combining 21-cm observations with other high- z probes to constrain the astrophysics of galaxies.

Key words: cosmology: theory – dark ages, reionisation, first stars – diffuse radiation – early Universe – galaxies: high-redshift – intergalactic medium

1 INTRODUCTION

The Epoch of Reionisation (EoR) corresponds to the final major baryonic phase change of the Universe. This occurs when the once cold, neutral hydrogen that permeated the

* E-mail: greigb@unimelb.edu.au

early Universe following recombination is ionised by the cumulative ionising radiation from astrophysical sources (e.g. stars and galaxies). Observing this phase transition is vitally important, as it reveals insights into the nature, growth and structure of the first astrophysical sources. These properties can be indirectly inferred through the imprint of their radiation on the intergalactic medium (IGM).

The ubiquity of neutral hydrogen in the early Universe should allow us to detect the imprint of the EoR through the 21-cm hyperfine transition (see e.g. Furlanetto et al. 2006; Morales & Wyithe 2010; Pritchard & Loeb 2012; Zaroubi 2013; Barkana 2016). This 21-cm signal is sensitive both to the thermal and ionisation state of the neutral hydrogen in the IGM. Further, being a line transition, the spatial and frequency (redshift) dependence of the 21-cm signal will reveal a full three dimensional picture of the IGM. Ultimately, the detection of this 21-cm signal will thus enable us to infer the ultra-violet (UV) and X-ray properties of the astrophysical sources responsible for reionisation.

Unfortunately, the cosmic 21-cm signal is extremely faint, buried beneath astrophysical foregrounds which can be up to five orders of magnitude brighter. However, this has not deterred numerous observational efforts to measure this elusive signal. Broadly speaking, these can be separated into two classes of experiments: (i) large-scale interferometer experiments designed to measure the spatial fluctuations in the cosmic 21-cm signal and (ii) global signal experiments which average the signal over the entire visible sky.

Several large-scale radio interferometers have been constructed or proposed. The first generation of these experiments, the Low-Frequency Array (LOFAR; van Haarlem et al. 2013), the Murchison Wide Field Array (MWA; Tingay et al. 2013), the Precision Array for Probing the Epoch of Reionisation (PAPER; Parsons et al. 2010) and the upgraded Giant Metrewave Radio Telescope (uGMRT; Gupta et al. 2017) have limited sensitivities, requiring several years of observing time to potentially make a low signal-to-noise statistical detection of the signal. Second generation experiments, with considerably higher expected sensitivities, such as the Hydrogen Epoch of Reionization Array (HERA; DeBoer et al. 2017) and the Square Kilometre Array (SKA; Mellema et al. 2013; Koopmans et al. 2015) should be able to provide higher signal-to-noise statistical detections across multiple redshifts. Further, the SKA has been designed to be able to provide the first three-dimensional tomographic images of the EoR.

Somewhat easier to design and operate, there have also been numerous global experiments. These include, the Experiment to Detect the Global EoR Signature (EDGES; Bowman & Rogers 2010), the Sonda Cosmológica de las Islas para la Detección de Hidrógeno Neutro (SCI-HI; Voytek et al. 2014), the Shaped Antenna measurement of the background RAdio Spectrum (SARAS; Patra et al. 2015), Broadband Instrument for Global HyDrOgen ReioNisation Signal (BIGHORNS; Sokolowski et al. 2015), the Large Aperture Experiment to detect the Dark Ages (LEDA; Greenhill & Bernardi 2012; Bernardi et al. 2016a), Probing Radio Inten-

sity at high-Z from Marion (PRI^ZM; Philip et al. 2019) and the Netherlands-China Low-Frequency Explorer (NCLE¹).

Despite the wealth of experimental efforts to measure the cosmic 21-cm signal from the early Universe, there has only been one claimed detection during the cosmic dawn, an absorption feature in the global signal near $z \approx 17$ announced by EDGES (Bowman et al. 2018a). However, the cosmological origin of this signal is heavily disputed in the literature (see e.g. Hills et al. 2018; Draine & Miralda-Escudé 2018; Bowman et al. 2018b; Bradley et al. 2019; Singh & Subrahmanyan 2019) and requires confirmation by an independent experiment.

All other attempts to measure the cosmic 21-cm signal have resulted in upper limits on the signal amplitude. For global experiments, these correspond to limits on the overall sky-averaged brightness temperature, with best available limits available from LEDA (Bernardi et al. 2016b), EDGES high-band (Monsalve et al. 2017) and SARAS2 (Singh et al. 2017). In this work, we are specifically interested in the upper limits on the 21-cm power spectrum (PS), as this is a more information rich statistic.

The first upper limits on the 21-cm PS were measured by the Giant Metrewave Radio Telescope (GMRT; Paciga et al. 2013) at $z \approx 8.6$. Since then, each of the first generation of radio interferometers have all reported upper limits on the 21-cm PS. For LOFAR, these include single-night observations at $z = 9.6 - 10.6$ (Patil et al. 2017) and more recently, upper limits at $z = 19.8 - 25.2$ targeting the dark ages and cosmic dawn with the LOFAR-Low Band Antenna array (Gehlot et al. 2019). Recently, the completed PAPER experiment revised their best upper limits (Cheng et al. 2018; Kolopanis et al. 2019) across $z \approx 7.5 - 11$ following identification of issues in dealing with signal loss from earlier reported limits (Ali et al. 2015). Finally, the MWA recently reported their best upper limits at $z = 6.5 - 8.7$ from four seasons of observations (Trott et al. 2020), improving on previous measurements in the literature (Dillon et al. 2015; Beardsley et al. 2016; Barry et al. 2019; Li et al. 2019). In addition to these, the Owens Valley Radio Observatory Long Wavelength Array (OVRO-LWA; Eastwood et al. 2019) have also published upper limits at $z \approx 18.4$.

With Mertens et al. (2020), LOFAR has now considerably improved their best upper limits on the EoR using 141 hours of observations at $z \approx 9.1$ to achieve a 2σ upper limit on the 21-cm PS of $\Delta_{21}^2 \approx (73 \text{ mK})^2$ at $k \approx 0.075 h \text{ Mpc}^{-1}$. This corresponds to an improvement by a factor of ≈ 8 compared to their previous best upper limit (Patil et al. 2017). While such limits are still several orders of magnitude above fiducial theoretical models (e.g. Mesinger et al. 2016), they are aggressive enough to begin to rule out extreme models of reionisation known as ‘cold’ reionisation (e.g. Mesinger et al. 2013; Parsons et al. 2014). Here, ‘cold’ reionisation refers to models in which the IGM undergoes little to no heating, adiabatically cooling faster than the cosmic microwave background (CMB) as the Universe expands. This can result in large contrasts between the ionised and neutral IGM, driving 21-cm PS amplitudes in excess of $\Delta_{21}^2 \gtrsim 10^4 \text{ mK}^2$. Attempts to rule out such extreme regions of astrophysi-

¹ <https://www.isispace.nl/projects/ncle-the-netherlands-china-low-frequency-explorer/>

cal parameter space have already been explored for EDGES High-band (Monsalve et al. 2017, 2018, 2019) and the now retracted upper limits from PAPER (Pober et al. 2015; Greig et al. 2016).

A related study using these new LOFAR upper limits was already performed by Ghara et al. (2020)², using a different astrophysical model and semi-numerical simulation, GRIZZLY (Ghara et al. 2015, 2018). Their focus was on general IGM properties, such as the mean IGM neutral fraction and spin temperature. For their Monte-Carlo Markov Chain (MCMC) results they trained a 21-cm PS emulator and emulators connecting the source properties to the IGM properties. In this work, we use a galaxy model (e.g. Park et al. 2019) which allows us to directly compare against observations of the ultra-violet (UV) luminosity functions (LFs), as well as other observations of the first billion years. Thus, we place the recent LOFAR upper limits into context with other observational probes, finding that all models currently excluded by these new 21-cm upper limits are also excluded by existing probes, thereby strengthening each others individual evidence and solidly excluding extremely cold IGM models. Our framework directly forward models the 3D 21-cm signal. Thus the inferred, marginalised IGM properties can serve as tests of emulator-based MCMCs, as well as confirming the robustness of the conclusions to the choice of simulation tool.

The outline of the remainder of this paper is as follows. In Section 2, we summarise the astrophysical model used in this analysis, as well as the 21CMMC setup. In Section 3, we discuss our main results and in Section 4, we provide our conclusions. Unless otherwise noted, all quoted quantities are in co-moving units with the following adopted cosmological parameters: $(\Omega_\Lambda, \Omega_M, \Omega_b, n, \sigma_8, H_0) = (0.69, 0.31, 0.048, 0.97, 0.81, 68 \text{ km s}^{-1} \text{ Mpc}^{-1})$, consistent with recent results from the Planck mission (Planck Collaboration XIII 2016).

2 METHODOLOGY

2.1 Simulating the 21-cm signal

We simulate the cosmic 21-cm signal using the semi-numerical simulation code 21CMFAST³ (Mesinger & Furlanetto 2007; Mesinger et al. 2011). Specifically, we employ the most up-to-date astrophysical parameterisation (Park et al. 2019), which allows the star-formation rate and ionising escape fraction to be dependent on the host dark matter halo. This, through simple conversions, allows 21CMFAST to directly compute UV LFs which can be compared against observed high- z galaxy LFs.

It is important to note that this parameterisation is a simplification of the true underlying astrophysics describing the ionising sources. It assumes only a single population of ionising sources (i.e. a single power-law relation with

halo mass) and ignores any explicit redshift dependence on the escape fraction or stellar mass. Therefore, any conclusions drawn from this work are specific to the assumptions used in this source modelling. However, for the bulk of the galaxy population (i.e. $M_{UV} > -20$) the simple Park et al. (2019) parameterisation is consistent with both observations of high- z LFs as well as semi-analytical galaxy formation models and hydrodynamical simulations (e.g. Harikane et al. 2016; Mutch et al. 2016; Xu et al. 2016; Tacchella et al. 2018; Behroozi et al. 2019; Yung et al. 2019; Gillet et al., in prep). As such, there is currently no evidence that a more complicated source model is required at this stage. If more complex modelling is required, these existing parameters can be treated as effective, population averaged quantities. In the future, we can increase the source model complexity and use Bayesian evidence from our forward-modelling approach to quantify whether redshift-dependence is required by the observational data.

Finally, we adopt the on-the-fly ionising photon non-conservation correction (Park et al., in prep) which accounts for the fact that the excursion-set formalism used for tracking ionisations is not photon conserving in three dimensions (e.g. McQuinn et al. 2005; Zahn et al. 2007; Paranjape & Choudhury 2014; Paranjape et al. 2016; Hassan et al. 2017; Choudhury & Paranjape 2018; Hutter 2018; Molaro et al. 2019). Below we summarise the main ingredients of 21CMFAST and the corresponding astrophysical parameterisation, and refer the reader to the aforementioned works for further details.

2.1.1 Galaxy UV properties

It is assumed that the typical stellar mass of a galaxy, M_* , can be directly related to its host halo mass, M_h (e.g. Kuhlen & Faucher-Giguère 2012; Dayal et al. 2014; Behroozi & Silk 2015; Mitra et al. 2015; Mutch et al. 2016; Sun & Furlanetto 2016; Yue et al. 2016) through a power-law relation⁴ normalised to a dark matter halo of mass $10^{10} M_\odot$:

$$M_*(M_h) = f_* \left(\frac{\Omega_b}{\Omega_M} \right) M_h, \quad (1)$$

where f_* is the fraction of galactic gas in stars,

$$f_* = f_{*,10} \left(\frac{M_h}{10^{10} M_\odot} \right)^{\alpha_*}, \quad (2)$$

with $f_{*,10}$ being the normalisation of the relation and α_* its power-law index.

The star-formation rate (SFR) can then be estimated by dividing the stellar mass by a characteristic time-scale,

$$\dot{M}_*(M_h, z) = \frac{M_*}{t_* H^{-1}(z)}, \quad (3)$$

where $H^{-1}(z)$ is the Hubble time and t_* is a free parameter allowed to vary between zero and unity.

² While this work was nearing competition, a similar study by (Mondal et al. 2020) was published, focusing on placing limits on the contribution to the excess radio background from the high- z Universe. These authors also used 21-cm PS emulators to explore a large parameter space of models. Under circumstances when the model assumptions are similar, our results are broadly consistent.

³ <https://github.com/andreimesinger/21cmFAST>

⁴ At $z \gtrsim 5$ this power-law dependence between stellar mass and halo mass is consistent with the mean relation from semi-analytic model predictions (e.g. Mutch et al. 2016; Yung et al. 2019) and semi-empirical fits to observations (e.g. Harikane et al. 2016; Tacchella et al. 2018; Behroozi et al. 2019).

Equivalently, the UV ionising escape fraction, f_{esc} , is also parameterised to vary with halo mass,

$$f_{\text{esc}} = f_{\text{esc},10} \left(\frac{M_{\text{h}}}{10^{10} M_{\odot}} \right)^{\alpha_{\text{esc}}}, \quad (4)$$

with $f_{\text{esc},10}$ again normalised at a halo of mass $10^{10} M_{\odot}$ with the power-law index, α_{esc} .

Finally, to mimic the inability of small mass halos to host active, star-forming galaxies (i.e. because of inefficient cooling and/or feedback processes), a duty-cycle is included to suppress their contribution:

$$f_{\text{duty}} = \exp \left(- \frac{M_{\text{turn}}}{M_{\text{h}}} \right). \quad (5)$$

In effect, some fraction, $(1 - f_{\text{duty}})$, of dark matter haloes with mass M_{h} are unable to host star-forming galaxies, with the characteristic scale for this suppression being set by M_{turn} (e.g. Shapiro et al. 1994; Giroux et al. 1994; Hui & Gnedin 1997; Barkana & Loeb 2001; Springel & Hernquist 2003; Mesinger & Dijkstra 2008; Okamoto et al. 2008; Sobacchi & Mesinger 2013a,b).

In summary, this results in six free parameters describing the UV galaxy properties in our model, $f_{*,10}$, $f_{\text{esc},10}$, α_* , α_{esc} , M_{turn} and t_* .

2.1.2 Galaxy X-ray properties

Prior to reionisation, it is thought that the IGM undergoes heating in the early Universe due to X-rays. The likely, dominant source of these X-rays are stellar remnants within the first galaxies. In 21CMFAST, X-ray heating is included by calculating the cell-by-cell angle-averaged specific X-ray intensity, $J(\mathbf{x}, E, z)$, (in $\text{erg s}^{-1} \text{keV}^{-1} \text{cm}^{-2} \text{sr}^{-1}$), by integrating the co-moving X-ray specific emissivity, $\epsilon_{\text{X}}(\mathbf{x}, E_e, z')$ back along the light-cone:

$$J(\mathbf{x}, E, z) = \frac{(1+z)^3}{4\pi} \int_z^{\infty} dz' \frac{cdt}{dz'} \epsilon_{\text{X}} e^{-\tau}, \quad (6)$$

where $e^{-\tau}$ accounts for attenuation by the IGM. The co-moving specific emissivity, evaluated in the emitted frame, $E_e = E(1+z)/(1+z)$, is,

$$\epsilon_{\text{X}}(\mathbf{x}, E_e, z') = \frac{L_{\text{X}}}{\text{SFR}} \left[(1 + \bar{\delta}_{\text{nl}}) \int_0^{\infty} dM_{\text{h}} \frac{dn}{dM_{\text{h}}} f_{\text{duty}} \dot{M}_{*} \right], \quad (7)$$

where $\bar{\delta}_{\text{nl}}$ is the mean, non-linear density in a shell around (\mathbf{x}, z) and the quantity in square brackets is the SFR density along the light-cone.

The normalisation, L_{X}/SFR ($\text{erg s}^{-1} \text{keV}^{-1} M_{\odot}^{-1} \text{yr}$), is the specific X-ray luminosity per unit star formation escaping the host galaxies. This is assumed to be a power-law with respect to photon energy, $L_{\text{X}} \propto E^{-\alpha_{\text{X}}}$, which is attenuated below a threshold energy, E_0 , where photons are absorbed inside the host galaxy. The specific luminosity is then normalised to an integrated soft-band ($< 2 \text{ keV}$) luminosity per SFR (in $\text{erg s}^{-1} M_{\odot}^{-1} \text{yr}$), which is taken to be a free parameter:

$$L_{\text{X}<2 \text{ keV}}/\text{SFR} = \int_{E_0}^{2 \text{ keV}} dE_e L_{\text{X}}/\text{SFR}. \quad (8)$$

This limit of 2 keV approximates to an X-ray mean-free path of roughly the Hubble length at high redshifts, implying

harder photons do not contribute to heating the IGM (e.g. McQuinn 2012).

In summary, we have three free parameters describing the X-ray properties, $L_{\text{X}<2 \text{ keV}}/\text{SFR}$, E_0 and α_{X} .

2.1.3 Ionisation and thermal state of the IGM

The evolved density and velocity fields in 21CMFAST are obtained following second-order Lagrange perturbation theory (e.g. Scoccimarro 1998). Reionisation is then determined from the evolved density field by tracking the balance between the cumulative number of ionising photons against the number of neutral hydrogen atoms plus cumulative recombinations in spheres of decreasing radii. Each cell is flagged as ionised when,

$$n_{\text{ion}}(\mathbf{x}, z|R, \delta_R) \geq (1 + \bar{n}_{\text{rec}})(1 - \bar{x}_e), \quad (9)$$

where \bar{n}_{rec} is the cumulative number of recombinations (e.g. Sobacchi & Mesinger 2014) and n_{ion} is the cumulative number of IGM ionising photons per baryon inside a spherical region of size, R and corresponding overdensity, δ_R ,

$$n_{\text{ion}} = \bar{\rho}_b^{-1} \int_0^{\infty} dM_{\text{h}} \frac{dn(M_{\text{h}}, z|R, \delta_R)}{dM_{\text{h}}} f_{\text{duty}} \dot{M}_{*} f_{\text{esc}} N_{\gamma/b}, \quad (10)$$

where $\bar{\rho}_b$ is the mean baryon density and $N_{\gamma/b}$ is the number of ionising photons per stellar baryon⁵. The final term of Equation 9, $(1 - \bar{x}_e)$, corresponds to ionisations by X-rays, which are expected to contribute at the ~ 10 per cent level (e.g. Ricotti & Ostriker 2004; Mesinger et al. 2013; Madau & Fragos 2017; Ross et al. 2017; Eide et al. 2018).

The thermal state of the neutral IGM (and its partial ionisations) are tracked in each cell by following adiabatic heating/cooling, Compton heating/cooling, heating through partial ionisations, as well as the heating/ionisations from X-rays (discussed in the previous section). Combining all these, the IGM spin temperature, T_{S} , is then computed as a weighted mean between the gas and CMB temperatures, depending on the density and local Lyman- α ($\text{Ly}\alpha$) intensity impinging on each cell (Wouthuysen 1952; Field 1958).

This $\text{Ly}\alpha$ background (see e.g. Mesinger et al. 2011 for further details) is estimated by summing the contribution from: (i) excitations of neutral hydrogen by X-rays ($J_{\alpha,\text{X}}$) and (ii) direct stellar emission of photons between $\text{Ly}\alpha$ and the Lyman limit ($J_{\alpha,*}$). For (i), this is set by the X-ray heating rate assuming that energy injection is balanced by photons redshifting out of $\text{Ly}\alpha$ resonance (Pritchard & Furlanetto 2007). For (ii), any Lyman- n resonance photons absorbed by the neutral IGM cascade with a recycling fraction passing through $\text{Ly}\alpha$ producing a background that is the sum over all Lyman resonances (e.g. Barkana & Loeb 2005). Note, the soft UV spectra of the stellar emission component of the first sources is currently held fixed and we do not include other possible sources of soft UV, such as quasars (see e.g. Qin et al. 2017; Ricci et al. 2017; Mitra et al. 2018).

⁵ We adopt a value of 5000, corresponding to a Salpeter initial mass function (Salpeter 1955); however note that this is highly degenerate with f_* .

2.1.4 Ionising photon non-conservation correction

As 21CMFAST employs an excursion-set formalism for determining which cells are ionised, it is impacted by the resultant non-conservation of ionising photons. This arises within cells that exceed the ionisation criteria (Eq. 9), where the excess ionising photons that are left over after ionising the neutral hydrogen are not propagated onward. This behaviour acts as an effective bias on the ionising escape fraction, f_{esc} . Roughly speaking, this corresponds to a loss of $\sim 10 - 20$ per cent of the ionising photons (e.g. McQuinn et al. 2005; Zahn et al. 2007; Paranjape & Choudhury 2014; Paranjape et al. 2016; Hassan et al. 2017; Choudhury & Paranjape 2018; Hutter 2018; Molaro et al. 2019).

Both Choudhury & Paranjape (2018) and Molaro et al. (2019) have introduced new, explicitly photon conserving algorithms for semi-numerical simulations. While being orders of magnitude faster than full radiative-transfer simulations, they are still considerably slower than conventional semi-numerical simulations. Under Bayesian parameter estimation approaches such as 21CMMC, these schemes are still intractable when forward modelling the 21-cm signal in the high-dimensional parameter spaces required to characterise the ionising, soft UV, and X-ray properties of the first galaxies.

Instead, Park et al., in prep, introduce an approximate correction to the ionising photon non-conservation issue, correcting for the effective bias on f_{esc} by analytically solving for the correct evolution of the ionisation fraction for a given source model, under the assumption of no correlations between the sources and sinks (which should only impact the final ~ 10 per cent of the EoR; Sobacchi & Mesinger 2014).

This analytic solution is compared against a calibration curve from 21CMFAST considering only ionisations (i.e. no recombinations or spin temperature evolution). If photons were conserved, these two curves would be identical. However, in practice the 21CMFAST history is delayed due to the loss of ionising photons. In order to recalibrate 21CMFAST, we decrease the redshift used for determining the ionisation field⁶. Note, this modified redshift is only used for modifying the ionisation field, all other quantities are calculated at the original redshift. We find that for the bulk of the EoR this corresponds roughly to a shift in redshift of $\Delta z \sim 0.3 \pm 0.1$.

2.1.5 Computing the 21-cm signal

Combining all the cosmological fields discussed in the previous section, we compute the observable cosmic 21-cm signal as a brightness temperature contrast relative to the CMB temperature, T_{CMB} (e.g. Furlanetto et al. 2006):

$$\delta T_{\text{b}}(\nu) = \frac{T_{\text{S}} - T_{\text{CMB}}(z)}{1+z} (1 - e^{-\tau_{\nu_0}}) \text{ mK}, \quad (11)$$

⁶ This effectively amounts to boosting the number of ionisations to compensate for the ionising photon non-conservation. However, we do not know *a-priori* how much to boost ionisations by, thus we modify the redshift to allow our calculation to be performed on-the-fly.

where τ_{ν_0} is the optical depth of the 21-cm line,

$$\tau_{\nu_0} \propto (1 + \delta_{\text{nl}})(1+z)^{3/2} \frac{x_{\text{HI}}}{T_{\text{S}}} \left(\frac{H}{dv_{\text{r}}/dr + H} \right). \quad (12)$$

Here, x_{HI} is the neutral hydrogen fraction, $\delta_{\text{nl}} \equiv \rho/\bar{\rho} - 1$ is the gas over-density, $H(z)$ is the Hubble parameter, dv_{r}/dr is the gradient of the line-of-sight component of the velocity and T_{S} is the gas spin temperature. All quantities are evaluated at redshift $z = \nu_0/\nu - 1$, where ν_0 is the 21-cm frequency and we drop the spatial dependence for brevity. Additionally, we include the impact of redshift space distortions along the line-of-sight as outlined in Mao et al. (2012); Jensen et al. (2013); Greig & Mesinger (2018).

2.2 Astrophysical parameter set

Under the assumptions of the adopted astrophysical model described previously, we have nine astrophysical parameters. Below, we summarise each of these and the associated parameter ranges we adopt based on previous explorations with 21CMMC (Greig et al. 2017; Park et al. 2019). We additionally summarise these in the top row of Table 1. Within 21CMMC we adopt flat priors over all of these parameter ranges.

(i) $f_{*,10}$: normalisation for the fraction of galactic gas in stars evaluated at a halo mass of $10^{10} M_{\odot}$. This is allowed to vary in the log as, $\log_{10}(f_{*,10}) \in [-3, 0]$.

(ii) α_* : power-law index for the star-formation as a function of halo mass, allowed to vary between, $\alpha_* \in [-0.5, 1]$.

(iii) $f_{\text{esc},10}$: normalisation for the ionising UV escape fraction evaluated at a halo mass of $10^{10} M_{\odot}$. We vary this in the log range, $\log_{10}(f_{\text{esc},10}) \in [-3, 0]$.

(iv) α_{esc} : power-law index for the ionising UV escape fraction as a function of halo mass, allowed to vary in the range, $\alpha_{\text{esc}} \in [-1, 0.5]$.

(v) t_* : the star-formation time scale as a fraction of the Hubble time, allowed to vary in the range, $t_* \in (0, 1]$.

(vi) M_{turn} : halo mass turn-over below which the abundance of active star-forming galaxies is exponentially suppressed by the adopted duty cycle. This is allowed to vary within the range, $\log_{10}(M_{\text{turn}}) \in [8, 10]$.

(vii) E_0 : the minimum energy threshold for X-ray photons capable of escaping their host galaxy. Allowed to vary within the range, $E_0 \in [0.2, 1.5]$ keV, which corresponds of an integrated column density of, $\log_{10}(N_{\text{HI}}/\text{cm}^2) \in [19.3, 23.0]$.

(viii) $L_{X<2\text{keV}}/\text{SFR}$: the normalisation for the soft-band X-ray luminosity per unit star-formation determined over the $E_0 - 2$ keV energy band. Allowed to vary across, $\log_{10}(L_{X<2\text{keV}}/\text{SFR}) \in [30, 42]$. Here, we considerably reduce the lower bound for $L_{X<2\text{keV}}/\text{SFR}$ compared to what is typically chosen (i.e. Park et al. 2019) in-order to explore truly ‘cold’ reionisation scenarios.

(iv) α_{X} : the power-law index for the SED of X-ray sources, which we allow to vary between $\alpha_{\text{X}} \in [-1, 3]$.

2.3 21CMMC setup

21CMMC⁷ is a massively parallel MCMC sampler of 3D semi-numerical reionisation simulations (Greig & Mesinger

⁷ <https://github.com/BradGreig/21CMMC>

2015, 2017; Greig & Mesinger 2018; Park et al. 2019). It is based on the PYTHON module COSMOHAMMER (Akeret et al. 2013) which uses the EMCEE PYTHON module (Foreman-Mackey et al. 2013), an affine invariant ensemble sampler from Goodman & Weare (2010). At each proposal step, 21CMMC performs an independent 3D realisation of the 21-cm signal using 21CMFAST to obtain a sampled 21-cm PS.

Typically, we would perform our MCMC seeking to maximise the likelihood that our astrophysical model is consistent with the observational data. However, current upper limits on the 21-cm signal are not strong enough to yield statistically significant constraints on the astrophysical parameter space. Instead, following Ghara et al. (2020), we invert the typical problem by reversing the likelihood, maximising models which exceed the observational limits⁸. This enables us to explore the regions of astrophysical parameter space inconsistent with the recent LOFAR upper limits at $z \approx 9.1$. In this work, we model the likelihood as a one-sided Gaussian⁹ for each of the Fourier, k , data points quoted in Mertens et al. (2020). Therefore, our likelihood¹⁰, \mathcal{L} , is a product over all Fourier bins, k :

$$\mathcal{L} = \prod_i^n \left\{ \begin{array}{ll} 0 & \Delta_{21,m}^2 < \Delta_{21,d}^2 \\ 1 - \exp \left[-\frac{1}{2} \left(\frac{\Delta_{21,m}^2 - \Delta_{21,d}^2}{\sigma_i} \right)^2 \right] & \Delta_{21,m}^2 \geq \Delta_{21,d}^2 \end{array} \right. \quad (13)$$

where $\Delta_{21,m}^2$ and $\Delta_{21,d}^2$ correspond to the 21-cm PS from the astrophysical model sampled in 21CMMC and the LOFAR upper limits, respectively¹¹. Note, we have dropped the Fourier dependence from these terms, i.e. $\Delta_{21,m}^2 = \Delta_{21,m}^2(k_i)$, for brevity. This likelihood is then interpreted as:

- astrophysical models below the upper limit (i.e. $\Delta_{21,m}^2 < \Delta_{21,d}^2$) are perfectly consistent with the LOFAR upper limits and are thus given a likelihood of zero.
- above the upper limit (i.e. $\Delta_{21,m}^2 \geq \Delta_{21,d}^2$) the likelihood smoothly transitions from zero following a one-sided Gaussian of width equal to the total uncertainty, σ , on the

⁸ This approach corresponds to identifying models ruled out by LOFAR in order to allow our forward modelling approach to converge quicker.

⁹ Our choice is motivated by the fact that we treat the measured data-points quoted in Mertens et al. (2020) as limits. This differs from Ghara et al. (2020) who adopt an error function centred on the actual data-point value. As a result, our likelihood is more conservative than that of Ghara et al. (2020), however, ultimately the differences between these approaches is negligible.

¹⁰ This choice of zero is motivated by the fact that we model our likelihood as a one-sided Gaussian. Any model below the upper limit is perfectly consistent with the data, and thus would normally have a likelihood of unity. However, since we are interested in models which instead exceed the upper limits, we then subtract by unity resulting in zero likelihood. Note, in practice we only evaluate the likelihood at $k \approx 0.075 h \text{ Mpc}^{-1}$ rather than evaluating the full product. This is motivated by the fact that all 21CMFAST models were found to be below the upper-limit at the second k -bin.

¹¹ Note that this assumes the sample variance error is Gaussian distributed, which is a reasonable approximation in the modest S/N regime relevant for current and upcoming observations (Mondal et al. 2017; Shaw et al. 2020).

upper limit measurement. This implies astrophysical models with amplitudes much larger than the limit are ruled-out with greater certainty than those close to the central-limit.

The total uncertainty, σ on the upper limit is the quadrature sum of the quoted uncertainty on the limit value from Mertens et al. (2020) and a conservative 20 per cent multiplicative modelling uncertainty on the sampled 21-cm PS within 21CMMC. This modelling uncertainty is motivated by approximations adopted in semi-numerical simulations relative to radiative-transfer simulations (e.g. Zahn et al. 2011; Ghara et al. 2018; Hutter 2018).

The largest scale probed by the LOFAR upper limits corresponds to $k \approx 0.075 h \text{ Mpc}^{-1}$, which is a factor of two larger than the typical sampling scale adopted in 21CMMC (i.e. $k = 0.1 - 1.0 \text{ Mpc}^{-1}$). Therefore, to adequately sample these much larger spatial scales, within 21CMMC we perform 3D realisations of the cosmic 21-cm signal in a box of 400 Mpc and 128 voxels per side-length¹². This corresponds to a resolution that is $\sim 3 \text{ Mpc}$ per voxel, slightly larger than the preferred resolution of 21CMFAST. However, we have performed convergence tests to verify that the increased resolution of $\sim 3 \text{ Mpc}$ per voxel does not alter the

3 RESULTS

3.1 Disfavoured parameters

In Figure 1, we present the marginalised one and two dimensional posterior distributions output from 21CMMC using the setup described in Section 2.3 for the nine input parameters outlined in Section 2.2. Note that these results are obtained using only the LOFAR upper limits, no other existing observational constraints are used. The resultant 68th and 95th percentile limits on these parameters disfavoured by the LOFAR limits are summarised in Table 1.

It is imperative to point out that here we are only exploring models which exceed the LOFAR upper limits at $z \approx 9.1$. Therefore, any non-zero regions of the marginalised posteriors correspond to models which are in excess of the LOFAR upper limits. This approach is more of a demonstration that: (i) LOFAR is already capable of ruling out some models and (ii) that forward modelled MCMC tools during the EoR such as 21CMMC are necessary for interpreting the results. Nevertheless, below we discuss some of the deductions that can be made from the existing LOFAR upper limits. Note again though, that these results are specific to the underlying assumptions of our source model.

The most interesting limit that we can discern from Figure 1 is that of the soft-band X-ray luminosity, $L_{X < 2 \text{ keV}}/\text{SFR}$. This directly controls the amount of heating that the IGM undergoes between the dark ages and reionisation and is responsible for the ‘cold’ reionisation scenarios. At 95 per cent confidence, we are able to place limits of $\log_{10}(L_{X < 2 \text{ keV}}/\text{SFR}) \lesssim 39.04$. These limits sit below those from local populations of star-forming galaxies (Mineo et al.

¹² For our simulation volume, we estimate a sample variance of ~ 13 per cent for the largest physical scale sampled by LOFAR (i.e. $k \approx 0.075 h \text{ Mpc}^{-1}$), which is well below that of the combined error from the observations and modelling uncertainty.

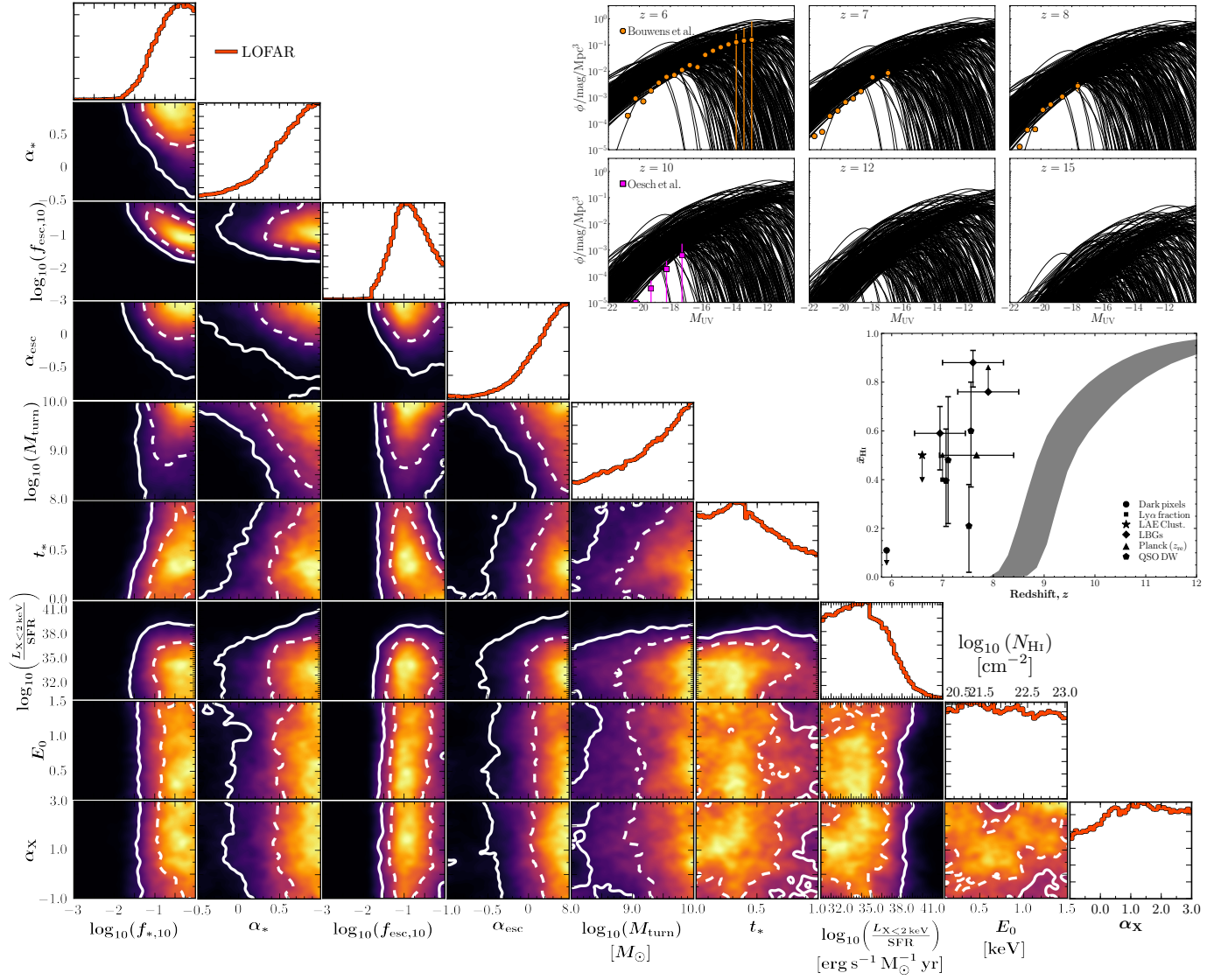


Figure 1. Marginalised one and two dimensional posterior distributions for the parameters which are disfavoured by just the LOFAR upper limits (i.e. no other observational probes) at $z \approx 9.1$ (Mertens et al. 2020). White dashed (solid) contours correspond to the 68th (95th) percentiles. In the top right panels, we provide 500 randomly sampled LFs which are drawn from the posterior of models that exceed the LOFAR upper limits and are compared against existing constraints at $z = 6 - 8$ (Bouwens et al. 2015, 2017) and $z = 10$ (Oesch et al. 2018). In the middle right panel, we compare the bounds on the reionisation histories disfavoured by LOFAR to all current observational constraints on the IGM neutral fraction (see text for further details).

	$\log_{10}(f_{*,10})$	α_*	$\log_{10}(f_{\text{esc},10})$	α_{esc}	$\log_{10}(M_{\text{turn}})$ [M_{\odot}]	t_*	$\log_{10}\left(\frac{L_{X<2\text{keV}}}{\text{SFR}}\right)$ [$\text{erg s}^{-1} M_{\odot}^{-1} \text{yr}$]	E_0 [keV]	α_X
Prior ranges	[-3.0, 0.0]	[-0.5, 1.0]	[-3.0, 0.0]	[-1.0, 0.5]	[8.0, 10.0]	(0.0, 1.0)	[30.0, 42.0]	[0.2, 1.5]	[-1.0, 3.0]
68th percentile limits	[-1.06, 0.0]	[0.28, 1.0]	[-1.27, -0.39]	[-0.11, 0.5]	[8.66, 10.0]	[0.0, 0.76]	[30, 36.58]	[0.2, 1.5]	[-0.2, 3.0]
95th percentile limits	[-1.53, 0.0]	[-0.23, 1.0]	[-1.64, 0.0]	[-0.64, 0.5]	[8.13, 10.0]	[0.0, 0.96]	[30, 39.04]	[0.2, 1.5]	[-0.87, 3.0]

Table 1. Summary of the 68th and 95th percentile limits on the disfavoured regions of nine astrophysical parameters included in 21CMMC using the LOFAR upper limits at $z \approx 9.1$ from Mertens et al. (2020).

2012), stacked *Chandra* observations (Lehmer et al. 2016) and predictions at high-redshifts by population synthesis models (Fragos et al. 2013). For the remaining two galaxy X-ray properties, E_0 and α_X we are currently unable to place any meaningful limits. This is driven by the fact that we

are ruling out models with little to no X-ray heating. In the absence of X-ray heating, it does not matter how much the X-ray SED is attenuated or its power-law shape.

For the galaxy UV properties, the limits are driven by the requirement to maximise the 21-cm PS amplitude at

$z \approx 9.1$ (to be able to exceed the LOFAR limit). This occurs when we are roughly at the mid-point of reionisation (i.e. $\bar{x}_{\text{HI}} \sim 0.5$) where the 21-cm PS peak is typically¹³ at its maximum (e.g. Mellema et al. 2006; Lidz et al. 2008). Therefore, the limits on $f_{*,10}$, α_* , $f_{\text{esc},10}$, α_{esc} and M_{turn} are completely degenerate. For $f_{\text{esc},10}$ we recover constraints on disallowed values, but for the remainder we only recover limits. This arises due to the completely degenerate nature between $f_{*,10}$ and $f_{\text{esc},10}$ for single redshift measurements and the absence of any other observational constraints (i.e. UV LFs, Park et al. 2019). Further contributing to this are the different prior ranges for the corresponding power-law indices α_* and α_{esc} . Nevertheless, these limits imply that LOFAR disfavors normalisations of the mass dependent star-formation rate, $f_{*,10}$ and escape fraction, $f_{\text{esc},10}$, to be above ~ 3.1 and ~ 2.3 per cent, respectively. Also, a minimum source mass above $\log_{10}(M_{\text{turn}}) \gtrsim 8.13$ is disfavoured at 95 per cent confidence.

Unfortunately, owing to differences in the choice of varied parameters (and their allowed ranges), their corresponding meaning (i.e. the mass dependence of star-formation rates and escape fractions in 21CMFAST), direct comparison to the results of Ghara et al. (2020) is not possible. However, the general trends of both this work and of Ghara et al. (2020) are consistent: (i) EoR to be ongoing at $z \approx 9.1$ disfavouring low mass star-forming galaxies and high ionising escape fractions and (ii) very low X-ray luminosities.

3.2 Comparison against existing observations

Next, we focus more on globally averaged quantities and how they compare against existing independent observations and limits in the literature.

3.2.1 Reionisation history

In the middle right panel of Figure 1 we present a census of all existing constraints on the IGM neutral fraction against the full range of reionisation histories disfavoured by LOFAR (shaded region). We compare against the dark pixel statistics of high- z quasars (QSOs; McGreer et al. 2015), Ly α fraction (Mesinger et al. 2015), the clustering of Ly α emitters (LAEs; Sobacchi & Mesinger 2015), the Ly α equivalent width distribution of Lyman-break galaxies (LBGs; Mason et al. 2018; Hoag et al. 2019; Mason et al. 2019), the neutral IGM damping wing imprint from high- z QSOs (Greig et al. 2017; Davies et al. 2018; Greig & Mesinger 2018) and the midpoint of reionisation (z_{Re}) from Planck (Planck Collaboration et al. 2018).

As discussed in the previous section, the models disfavoured by the LOFAR upper limits are driven to produce a midpoint of reionisation at $z \approx 9.1$. The full range of IGM neutral fractions disfavoured by LOFAR at $z \approx 9.1$ correspond to $0.15 \lesssim \bar{x}_{\text{HI}} \lesssim 0.6$. Compared to the existing

observational constraints, this places these disfavoured models at roughly $\gtrsim 2\sigma$. Unfortunately, owing to the still large amplitude of the LOFAR upper limits, and the correspondingly large uncertainties, we have verified that a joint analysis is entirely constrained by the existing limits. However, prospects for this will improve in the near future with the further processing of existing observational data and multiple frequency (redshift) limits.

Our constraints on \bar{x}_{HI} are broadly consistent with Ghara et al. (2020), with any differences being explained by different choices in adopted priors between the two works. The Ghara et al. (2020) limits on \bar{x}_{HI} appear from two regions of parameter space (c.f. their Table 5): (i) ‘cold’ reionisation ($0.40 < \bar{x}_{\text{HI}} < 0.55$) and (ii) patchy X-ray heating ($\bar{x}_{\text{HI}} > 0.92$). For (i), reionisation must be ongoing and the IGM must be cold. Our results are consistent with (i), given that Ghara et al. (2020) assume a fixed $M_{\text{turn}} = 10^9 M_{\odot}$ while also including a hard prior on the neutral fraction excluding values below 0.19, while we have a flat prior down to zero. For (ii), Ghara et al. (2020) require reionisation to be in its infancy and X-ray heating to be dominated by luminous, highly biased ($M_h \geq 10^{10} M_{\odot}$) sources with very soft SEDs ($E_0 = 0.2$ keV). We do not recover their (ii) because our prior on M_{turn} has a hard upper limit of $M_h \leq 10^{10} M_{\odot}$.

3.2.2 UV luminosity functions

Unlike the reionisation history which is constrained to be within a narrow range around $\bar{x}_{\text{HI}} \approx 0.5$, the UV LFs are not strongly constrained. Instead, they show extremely large scatter in the shapes and amplitudes, especially at the faint end. As such, we cannot simply provide a constrained range of plausible UV LFs as we did previously for the reionisation history (shaded region of middle right panel of Figure 1). Therefore, in the six panels in the top right of Figure 1 we plot the resultant UV luminosity functions at $z = 6, 7, 8, 10, 12$ and 15 for 500 randomly sampled models drawn from the posterior which exceed the LOFAR upper limit. This is one of the advantages of using 21CMFAST in that the built-in parameterisation is capable of directly outputting UV LFs.

We compare these UV LFs against existing observations from unlensed UV LFs at $z = 6 - 8$ (orange circles; Bouwens et al. 2015, 2017) and at $z = 10$ (pink squares; Oesch et al. 2018). The vast majority of the UV LFs disfavoured by LOFAR are strongly disfavoured by the existing UV galaxy limits (up to two orders of magnitude larger in amplitude). Again, this is driven by models producing excessive amounts of ionising photons to have reionisation ~ 50 per cent complete by $z \approx 9.1$. While the UV LFs are independent of the number of ionising photons, to achieve cold reionisation at $z \approx 9.1$ we prefer to have both a high f_{esc} and high stellar-to-halo mass relation (see the $f_* - f_{\text{esc}}$ panel in Figure 1). Interestingly, unlike the existing constraints on the IGM neutral fraction, there appear to be several models in excess of the LOFAR limits which appear to be capable of producing UV LFs consistent with the observed ones. However, the vast majority are strongly inconsistent, owing to the relatively small statistical uncertainties on the observed UV LFs.

Once again, this highlights the fundamental value of observing the cosmic 21-cm signal. Constraints on the amplitude of the 21-cm PS are capable of providing limits on

¹³ The peak amplitude of the 21-cm PS is actually strongly model dependent and need not occur at the mid-point of reionisation. However, throughout we refer to the peak occurring near the mid-point of reionisation purely for the purpose of making a generalised qualitative statement.

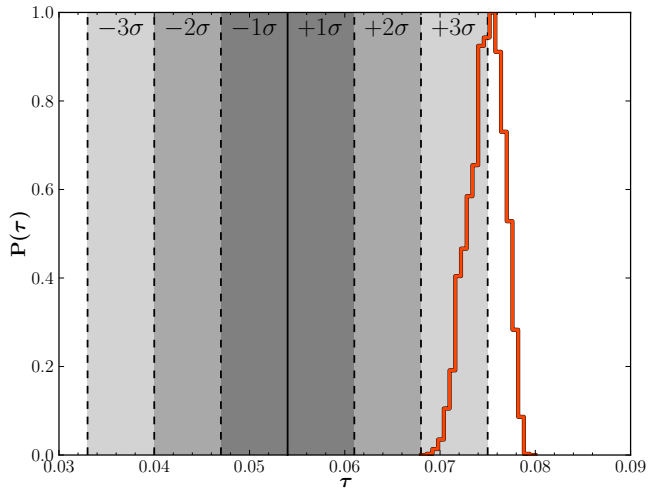


Figure 2. Histogram (red curve) of τ_e from all models found to be in excess of the LOFAR upper limits on the 21-cm PS at $z \approx 9.1$. Shaded bands correspond to the statistical uncertainty on τ_e as measured by Planck ($\tau_e = 0.054 \pm 0.007$; Planck Collaboration et al. 2018).

the underlying UV galaxy LFs, beyond what is capable from existing space telescopes. Our galaxy model, which has an average star-formation time-scale evolving with redshift as the Hubble time (or analogously the halo dynamical time; Equation 3), and a redshift-independent stellar-to-halo mass relation is capable of reproducing current observations of high- z (z 6-10) UV LFs (e.g. figure 4 of Park et al. 2019). Moreover, these scaling relations are consistent with more sophisticated high- z SAMs (e.g. Mutch et al. 2016; Yung et al. 2019), as well as empirical scaling relations (e.g. Tacchella et al. 2018). Therefore the fact that the UV LFs corresponding to the models inconsistent with the LOFAR observations are generally above the observed UV LFs is a significant result, highlighting that such models are already ruled out by current observations.

3.2.3 Electron scattering optical depth, τ_e

Next, in Figure 2 we consider the electron scattering optical depth, τ_e , using the latest constraints from Planck ($\tau_e = 0.054 \pm 0.007$; Planck Collaboration et al. 2018). Here, the solid vertical line is the mean value from Planck, with shaded regions corresponding to being within $\pm 1\sigma$, $\pm 2\sigma$, $\pm 3\sigma$ of the mean observed value. The red curve is the histogram of τ_e obtained by binning all models disfavoured by the LOFAR upper limits. Clearly, all models in excess of LOFAR are $\gtrsim 2\sigma$ from existing observational constraints. Note again, this arises owing to the assumptions of our astrophysical source parameterisation¹⁴. For example, allowing a strong redshift dependence on f_{esc} could

¹⁴ We note that our parametrisation does allow for the *population averaged* f_{esc} to vary with redshift. This is because the halo mass function evolves with redshift, and we allow f_{esc} to scale with the halo mass through a power law relation whose index, α_{esc} , is a free parameter. However, our range of priors on α_{esc} results in

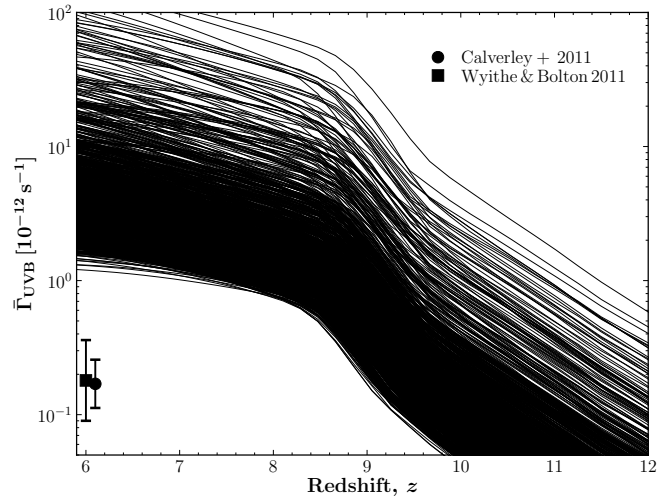


Figure 3. A comparison of the mean UV background radiation ($\bar{\Gamma}_{\text{UVB}}$) from a random sample of 500 models drawn from the posterior (black curves) in excess of the LOFAR 21-cm PS upper limits against observed constraints from the proximity zones of high- z quasars (Calverley et al. 2011; Wyithe & Bolton 2011).

produce models consistent with Planck. However, we note that most hydrodynamical simulations do not find evidence for a strong redshift evolution for f_{esc} (e.g. Kimm & Cen 2014; Paardekooper et al. 2015; Xu et al. 2016; Ma et al. 2020, though see Lewis et al. 2020). The primary driver of this is the requirement to have reionisation at ~ 50 per cent by $z \sim 9.1$ for the 21-cm signal to exceed the current LOFAR limits, whereas the observed values from Planck prefer a redshift for the mid-point of $z_{\text{Re}} = 7.67 \pm 0.5$ Planck Collaboration et al. 2018).

3.2.4 Mean UV photo-ionisation rate, $\bar{\Gamma}_{\text{UVB}}$

In Figure 3 we compare the mean UV background photoionisation rate from 500 randomly sampled models from the posterior in excess of the LOFAR upper limits to observational constraints extracted from the proximity zones of $z > 6$ QSOs (e.g. Calverley et al. 2011; Wyithe & Bolton 2011). Here, the vast majority of the models ruled out by LOFAR are at least two orders of magnitude larger in amplitude than those inferred from the observational constraints ($\gtrsim 3\sigma$). This is consistent with the picture of an excessive amount of ionising photons being required to ensure reionisation is ~ 50 per cent complete by $z \approx 9.1$. As a result, these models drastically overproduce the mean background photo-ionisation rate.

3.3 Disfavoured IGM properties

Finally, we directly investigate the inferred limits on the IGM spin temperature from the models found to be in excess of the LOFAR upper limits at $z \approx 9.1$. Note, these are

a relatively modest redshift evolution of the population averaged galaxy f_{esc} .

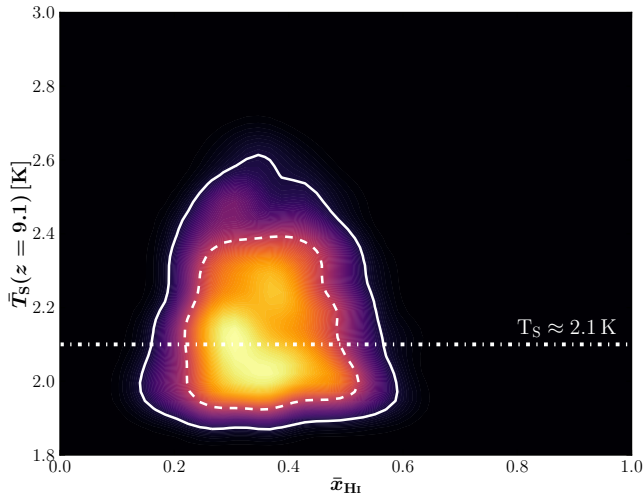


Figure 4. Two dimensional marginalised constraints on the IGM spin temperature, T_S , and the IGM neutral fraction, \bar{x}_{HI} . The white dashed (solid) contours corresponds to the 68th (95th) percentiles while the horizontal white dot-dashed line corresponds to the value of the adiabatically cooled neutral IGM gas at mean density from RECFAST.

derived limits obtained by marginalising over the full posterior of the model parameters. These limits are primarily driven by those models we rule out with extremely low soft-band X-ray luminosities (i.e. $\log_{10}(L_{X<2\text{keV}}/\text{SFR}) \lesssim 39.04$ from Section 3.1). In the absence of any heating source for the IGM, the neutral hydrogen gas will adiabatically cool. At $z \approx 9.1$, we infer this adiabatically cooled value for the neutral IGM gas at mean density to be $T_S \approx 2.1$ K (RECFAST; Seager et al. 1999, 2000).

In Figure 4 we provide the two dimensional marginalised posterior for the IGM spin temperature, T_S and the IGM neutral fraction, \bar{x}_{HI} after marginalising over all parameters outlined in Section 2.2. The horizontal dot-dashed line corresponds to the value of the adiabatically cooled neutral IGM at mean density, $T_S \approx 2.1$ K. Note, within 21CMFAST it is possible to have temperatures below $T_S \approx 2.1$ K. This arises owing to adiabatic cooling and Compton heating in a non-uniform IGM. Due to non-linear structure evolution (i.e. more volume is in voids than overdensities) the volume weighted T_S can be below the limit at mean density (i.e. $T_S \approx 2.1$ K). Figure 4 implies that over a IGM neutral fraction of $0.15 \lesssim \bar{x}_{\text{HI}} \lesssim 0.6$, the IGM spin temperature is disfavoured by LOFAR at 95 per cent confidence at $T_S \lesssim 2.6$ K. This implies that the IGM must have undergone, at the bare minimum, the slightest amount of heating by X-rays.

Ghara et al. (2020) quote their own 95 per cent disfavoured limit on the IGM spin temperature of $T_S \lesssim 2.9$ K, however, this is inferred from their uniform IGM spin temperature model (with their inhomogeneous limit instead expressed as a volume weighted fraction of heating). Nevertheless, this limit is broadly consistent with the limit from our own analysis using a non-uniform IGM spin temperature.

4 CONCLUSION

Recently, LOFAR published new upper limits on the 21-cm PS from 141 hours of data at $z \approx 9.1$ (Mertens et al. 2020). This corresponds to a factor ~ 8 improvement over their best previous upper limit (Patil et al. 2017). Using 21CMCMC, an MCMC sampler of 3D reionisation simulations, we explore regions of astrophysical parameter space that are inconsistent with the observed limits. We directly forward-model the 3D cosmic 21-cm signal which includes: (i) a mass-dependent star-formation rate and escape fraction to be able to self-consistently produce UV LFs, (ii) inhomogeneous recombinations, (iii) the evolution of the inhomogeneous IGM spin temperature and (iv) an on-the-fly ionising photon non-conservation corrections.

In terms of the astrophysical parameters responsible for reionisation, we find that the upper limits presented by LOFAR are able to primarily limit the X-ray luminosity of the first sources. At 95 per cent confidence, LOFAR disfavours the soft-band X-ray luminosity, $L_{X<2\text{keV}}/\text{SFR}$ to $\log_{10}(L_{X<2\text{keV}}/\text{SFR}) \lesssim 39.04$. These limits currently sit below expectations from local populations of star-forming galaxies (Mineo et al. 2012), stacked *Chandra* observations (Lehmer et al. 2016) and predictions at high-redshifts by population synthesis models (Fragos et al. 2013). Nevertheless, this implies that the X-ray background must have been sufficiently large to provide some level of heating to the IGM.

For the UV galaxy properties, we find that the regions disfavoured by LOFAR are heavily tied to the observational redshift of $z \approx 9.1$. That is, to be able to exceed the LOFAR upper limit, reionisation must have been ~ 50 per cent complete to maximise the amplitude of the 21-cm PS. As such, the LOFAR upper limits disfavour the normalisations of the mass dependent star-formation rate, $f_{*,10}$ and escape fraction, $f_{\text{esc},10}$, to be above ~ 3.1 and ~ 2.3 per cent, respectively. Finally, a minimum source mass above $\log_{10}(M_{\text{turn}}) \gtrsim 8.13$ is disfavoured at 95 per cent confidence. This shows the value of having tools such as 21CMCMC to perform forward modelling of the cosmic 21-cm signal to be able to infer the astrophysics from observations of the 21-cm signal in a fully Bayesian framework. Note however, this interpretation is specific to our astrophysical parameterisation.

To highlight the advantage of using 21CMCMC we then compared the models disfavoured by the LOFAR upper limits against a range of existing observation constraints within the literature. We compared against: (i) observational constraints and limits on the IGM neutral fraction, (ii) the observed UV LFs at $z = 6, 7, 8$ and 10, (iii) the electron scattering optical depth and (iv) the mean UV background photoionisation rate. In most instances the astrophysical models disfavoured by LOFAR were inconsistent with existing observational constraints by $\gtrsim 2\sigma$.

Finally, we explored limits on the IGM spin temperature, T_S , due to the lack of X-ray heating inferred in the models disfavoured by LOFAR. Over an IGM neutral fraction range of $0.15 \lesssim \bar{x}_{\text{HI}} \lesssim 0.6$, the LOFAR upper limits imply a 95 per cent confidence limit of $T_S \gtrsim 2.6$ K. In comparison, the adiabatically cooled limit at $z \approx 9.1$ is $T_S \approx 2.1$ K (at mean density), which implies the IGM must have undergone some level of X-ray heating. This interpretation is consistent with the results presented in Ghara et al. (2020)

and provides a consistency check that the recovered bulk IGM properties from the current LOFAR limits are insensitive to the details of the modelling, including the type of semi-numerical simulation, galaxy parametrisation, and use of emulators in the MCMC.

With the amplitude of the existing limits on the 21-cm PS presented by LOFAR still being relatively large, and only at a single observed frequency, this limits our ability to constrain the astrophysics of the sources responsible for reionisation. However, in the near future these limits will continue to reduce in amplitude as LOFAR processes more observational data and improves their analysis pipeline, while at the same time also providing multiple frequency limits. Using the framework showcased here, these upcoming limits can start ruling out otherwise viable galaxy evolution models.

ACKNOWLEDGEMENTS

Parts of this research were supported by the Australian Research Council Centre of Excellence for All Sky Astrophysics in 3 Dimensions (ASTRO 3D), through project number CE170100013. AM acknowledges funding support from the European Research Council (ERC) under the European Union's Horizon 2020 research and innovation programme (grant agreement No 638809 – AIDA – PI: AM). FGM and LVEK would like to acknowledge support from an SKA-NL Roadmap grant from the Dutch Ministry of Education, Culture and Science. GM is thankful for support by Swedish Research Council grant 2016-03581. SZ acknowledges support from the Israeli Science Foundation (grant no. 255/18). ITI was supported by the Science and Technology Facilities Council [grant numbers ST/I000976/1 and ST/T000473/1] and the Southeast Physics Network (SEP-Net).

REFERENCES

Akeret J., Seehars S., Amara A., Refregier A., Csillaghy A., 2013, *Astron. Comput.*, 2, 27
 Ali Z. S., et al., 2015, *ApJ*, 809, 61
 Barkana R., 2016, *Phys. Rep.*, 645, 1
 Barkana R., Loeb A., 2001, *Phys. Rep.*, 349, 125
 Barkana R., Loeb A., 2005, *ApJ*, 626, 1
 Barry N., et al., 2019, *ApJ*, 884, 1
 Beardsley A. P., et al., 2016, *ApJ*, 833, 102
 Behroozi P. S., Silk J., 2015, *ApJ*, 799, 32
 Behroozi P., Wechsler R. H., Hearin A. P., Conroy C., 2019, *MNRAS*, 488, 3143
 Bernardi G., et al., 2016a, *MNRAS*, 461, 2847
 Bernardi G., et al., 2016b, *MNRAS*, 461, 2847
 Bouwens R. J., et al., 2015, *ApJ*, 803, 34
 Bouwens R. J., Oesch P. A., Illingworth G. D., Ellis R. S., Stefanon M., 2017, *ApJ*, 843, 129
 Bowman J. D., Rogers A. E. E., 2010, *Nature*, 468, 796
 Bowman J. D., Rogers A. E. E., Monsalve R. A., Mozdzen T. J., Mahesh N., 2018a, *Nature*, 555, 67
 Bowman J. D., Rogers A. E. E., Monsalve R. A., Mozdzen T. J., Mahesh N., 2018b, *Nature*, 564, E35
 Bradley R. F., Tauscher K., Rapetti D., Burns J. O., 2019, *ApJ*, 874, 153
 Calverley A. P., Becker G. D., Haehnelt M. G., Bolton J. S., 2011, *MNRAS*, 412, 2543
 Cheng C., et al., 2018, *ApJ*, 868, 26
 Choudhury T. R., Paranjape A., 2018, *MNRAS*, 481, 3821

Davies F. B., et al., 2018, *ApJ*, 864, 142
 Dayal P., Ferrara A., Dunlop J. S., Pacucci F., 2014, *MNRAS*, 445, 2545
 DeBoer D. R., et al., 2017, *PASP*, 129, 045001
 Dillon J. S., et al., 2015, *Phys. Rev. D*, 91, 123011
 Draine B. T., Miralda-Escudé J., 2018, *ApJ*, 858, L10
 Eastwood M. W., et al., 2019, *AJ*, 158, 84
 Eide M. B., Graziani L., Ciardi B., Feng Y., Kakiichi K., Di Matteo T., 2018, *MNRAS*, 476, 1174
 Field G. B., 1958, *Proc. Inst. Radio Eng.*, 46, 240
 Foreman-Mackey D., Hogg D. W., Lang D., Goodman J., 2013, *PASP*, 125, 306
 Fragos T., et al., 2013, *ApJ*, 764, 41
 Furlanetto S. R., Oh S. P., Briggs F. H., 2006, *Phys. Rep.*, 433, 181
 Gehlot B. K., et al., 2019, *MNRAS*, 488, 4271
 Ghara R., Choudhury T. R., Datta K. K., 2015, *MNRAS*, 447, 1806
 Ghara R., Mellema G., Giri S. K., Choudhury T. R., Datta K. K., Majumdar S., 2018, *MNRAS*, 476, 1741
 Ghara R., et al., 2020, *MNRAS*, 493, 4728
 Giroux M. L., Sutherland R. S., Shull J. M., 1994, *ApJ*, 435, L97
 Goodman J., Weare J., 2010, *Commun. Appl. Math. Comput. Sci.*, 5, 1
 Greenhill L. J., Bernardi G., 2012, preprint (arXiv:1201.1700)
 Greig B., Mesinger A., 2015, *MNRAS*, 449, 4246
 Greig B., Mesinger A., 2017, *MNRAS*, 472, 2651
 Greig B., Mesinger A., 2018, *MNRAS*, 477, 3217
 Greig B., Mesinger A., Pober J. C., 2016, *MNRAS*, 455, 4295
 Greig B., Mesinger A., Haiman Z., Simcoe R. A., 2017, *MNRAS*, 466, 4239
 Gupta Y., et al., 2017, *Current Science*, 113, 707
 Harikane Y., et al., 2016, *ApJ*, 821, 123
 Hassan S., Davé R., Finlator K., Santos M. G., 2017, *MNRAS*, 468, 122
 Hills R., Kulkarni G., Meerburg P. D., Puchwein E., 2018, *Nature*, 564, E32
 Hoag A., et al., 2019, *ApJ*, 878, 12
 Hui L., Gnedin N. Y., 1997, *MNRAS*, 292, 27
 Hutter A., 2018, *MNRAS*, 477, 1549
 Jensen H., et al., 2013, *MNRAS*, 435, 460
 Kimm T., Cen R., 2014, *ApJ*, 788, 121
 Kolopanis M., et al., 2019, *ApJ*, 883, 133
 Koopmans L., et al., 2015, in *Advancing Astrophysics with the Square Kilometre Array (AASKA14)*, preprint (arXiv:1505.07568). (arXiv:1505.07568)
 Kuhlen M., Faucher-Giguère C.-A., 2012, *MNRAS*, 423, 862
 Lehmer B. D., et al., 2016, *ApJ*, 825, 7
 Lewis J. S. W., et al., 2020, preprint (arXiv:2001.07785),
 Li W., et al., 2019, *ApJ*, 887, 141
 Lidz A., Zahn O., McQuinn M., Zaldarriaga M., Hernquist L., 2008, *ApJ*, 680, 962
 Ma X., Quataert E., Wetzel A., Hopkins P. F., Faucher-Giguère C.-A., Kereš D., 2020, preprint (arXiv:2003.05945),
 Madau P., Fragos T., 2017, *ApJ*, 840, 39
 Mao Y., Shapiro P. R., Mellema G., Iliev I. T., Koda J., Ahn K., 2012, *MNRAS*, 422, 926
 Mason C. A., Treu T., Dijkstra M., Mesinger A., Trenti M., Pentericci L., de Barros S., Vanzella E., 2018, *ApJ*, 856, 2
 Mason C. A., et al., 2019, *MNRAS*, 485, 3947
 McGreer I. D., Mesinger A., D'Odorico V., 2015, *MNRAS*, 447, 499
 McQuinn M., 2012, *MNRAS*, 426, 1349
 McQuinn M., Furlanetto S. R., Hernquist L., Zahn O., Zaldarriaga M., 2005, *ApJ*, 630, 643
 Mellema G., Iliev I. T., Pen U.-L., Shapiro P. R., 2006, *MNRAS*, 372, 679
 Mellema G., et al., 2013, *Exp. Astron.*, 36, 235

- Mertens F. G., et al., 2020, *MNRAS*, **493**, 1662
- Mesinger A., Dijkstra M., 2008, *MNRAS*, **390**, 1071
- Mesinger A., Furlanetto S., 2007, *ApJ*, **669**, 663
- Mesinger A., Furlanetto S., Cen R., 2011, *MNRAS*, **411**, 955
- Mesinger A., Ferrara A., Spiegel D. S., 2013, *MNRAS*, **431**, 621
- Mesinger A., Aykutaalp A., Vanzella E., Pentericci L., Ferrara A., Dijkstra M., 2015, *MNRAS*, **446**, 566
- Mesinger A., Greig B., Sobacchi E., 2016, *MNRAS*, **459**, 2342
- Mineo S., Gilfanov M., Sunyaev R., 2012, *MNRAS*, **419**, 2095
- Mitra S., Choudhury T. R., Ferrara A., 2015, *MNRAS*, **454**, L76
- Mitra S., Choudhury T. R., Ferrara A., 2018, *MNRAS*, **473**, 1416
- Molaro M., Davé R., Hassan S., Santos M. G., Finlator K., 2019, *MNRAS*, **489**, 5594
- Mondal R., Bharadwaj S., Majumdar S., 2017, *MNRAS*, **464**, 2992
- Mondal R., et al., 2020, arXiv e-prints, p. [arXiv:2004.00678](https://arxiv.org/abs/2004.00678)
- Monsalve R. A., Rogers A. E. E., Bowman J. D., Mozdzen T. J., 2017, *ApJ*, **847**, 64
- Monsalve R. A., Greig B., Bowman J. D., Mesinger A., Rogers A. E. E., Mozdzen T. J., Kern N. S., Mahesh N., 2018, *ApJ*, **863**, 11
- Monsalve R. A., Fialkov A., Bowman J. D., Rogers A. E. E., Mozdzen T. J., Cohen A., Barkana R., Mahesh N., 2019, *ApJ*, **875**, 67
- Morales M. F., Wyithe J. S. B., 2010, *ARA&A*, **48**, 127
- Mutch S. J., Geil P. M., Poole G. B., Angel P. W., Duffy A. R., Mesinger A., Wyithe J. S. B., 2016, *MNRAS*, **462**, 250
- Oesch P. A., Bouwens R. J., Illingworth G. D., Labbé I., Stefanon M., 2018, *ApJ*, **855**, 105
- Okamoto T., Gao L., Theuns T., 2008, *MNRAS*, **390**, 920
- Paardekooper J.-P., Khochfar S., Vecchia C. D., 2015, *MNRAS*, **451**, 2544
- Paciga G., et al., 2013, *MNRAS*, **433**, 1174
- Paranjape A., Choudhury T. R., 2014, *MNRAS*, **442**, 1470
- Paranjape A., Choudhury T. R., Padmanabhan H., 2016, *MNRAS*, **460**, 1801
- Park J., Mesinger A., Greig B., Gillet N., 2019, *MNRAS*, **484**, 933
- Parsons A. R., et al., 2010, *AJ*, **139**, 1468
- Parsons A. R., et al., 2014, *ApJ*, **788**, 106
- Patil A. H., et al., 2017, *ApJ*, **838**, 65
- Patra N., Subrahmanyan R., Sethi S., Shankar N. U., Raghunathan A., 2015, *ApJ*, **801**, 138
- Philip L., et al., 2019, *Journal of Astronomical Instrumentation*, **8**, 1950004
- Planck Collaboration XIII 2016, *A&A*, **594**, A13
- Planck Collaboration et al., 2018, preprint (arXiv:1807.06209), p. [arXiv:1807.06209](https://arxiv.org/abs/1807.06209)
- Pober J. C., et al., 2015, *ApJ*, **809**, 62
- Pritchard J. R., Furlanetto S. R., 2007, *MNRAS*, **376**, 1680
- Pritchard J. R., Loeb A., 2012, *Rep. Prog. Phys.*, **75**, 086901
- Qin Y., et al., 2017, *MNRAS*, **472**, 2009
- Ricci F., Marchesi S., Shankar F., La Franca F., Civano F., 2017, *MNRAS*, **465**, 1915
- Ricotti M., Ostriker J. P., 2004, *MNRAS*, **350**, 539
- Ross H. E., Dixon K. L., Iliev I. T., Mellema G., 2017, *MNRAS*, **468**, 3785
- Salpeter E. E., 1955, *ApJ*, **121**, 161
- Scoccimarro R., 1998, *MNRAS*, **299**, 1097
- Seager S., Sasselov D. D., Scott D., 1999, *ApJ*, **523**, L1
- Seager S., Sasselov D. D., Scott D., 2000, *ApJS*, **128**, 407
- Shapiro P. R., Giroux M. L., Babul A., 1994, *ApJ*, **427**, 25
- Shaw A. K., Bharadwaj S., Mondal R., 2020, arXiv e-prints, p. [arXiv:2005.06535](https://arxiv.org/abs/2005.06535)
- Singh S., Subrahmanyan R., 2019, *ApJ*, **880**, 26
- Singh S., et al., 2017, *ApJL*, **845**, L12
- Sobacchi E., Mesinger A., 2013a, *MNRAS*, **432**, L51
- Sobacchi E., Mesinger A., 2013b, *MNRAS*, **432**, 3340
- Sobacchi E., Mesinger A., 2014, *MNRAS*, **440**, 1662
- Sobacchi E., Mesinger A., 2015, *MNRAS*, **453**, 1843
- Sokolowski M., et al., 2015, *PASA*, **32**, e004
- Springel V., Hernquist L., 2003, *MNRAS*, **339**, 312
- Sun G., Furlanetto S. R., 2016, *MNRAS*, **460**, 417
- Tacchella S., Bose S., Conroy C., Eisenstein D. J., Johnson B. D., 2018, *ApJ*, **868**, 92
- Tingay S. J., et al., 2013, *PASA*, **30**, 7
- Trott C. M., et al., 2020, *MNRAS*,
- Voytek T. C., Natarajan A., García J. M. J., Peterson J. B., López-Cruz O., 2014, *ApJL*, **782**, L9
- Wouthuysen S. A., 1952, *AJ*, **57**, 31
- Wyithe J. S. B., Bolton J. S., 2011, *MNRAS*, **412**, 1926
- Xu H., Wise J. H., Norman M. L., Ahn K., O'Shea B. W., 2016, *ApJ*, **833**, 84
- Yue B., Ferrara A., Xu Y., 2016, *MNRAS*, **463**, 1968
- Yung L. Y. A., Somerville R. S., Popping G., Finkelstein S. L., Ferguson H. C., Davé R., 2019, *MNRAS*, p. [2437](https://arxiv.org/abs/1907.04377)
- Zahn O., Lidz A., McQuinn M., Dutta S., Hernquist L., Zaldarriaga M., Furlanetto S. R., 2007, *ApJ*, **654**, 12
- Zahn O., Mesinger A., McQuinn M., Trac H., Cen R., Hernquist L. E., 2011, *MNRAS*, **414**, 727
- Zaroubi S., 2013, *The First Galaxies, Astrophysics and Space Science Library*, Vol. 396. Springer-Verlag, Berlin, p. 45
- van Haarlem M. P., et al., 2013, *A&A*, **556**, 2